Chemical Etching of Sb_2Se_3 Solar Cells: Surface Chemistry and Back Contact Behaviour

†‡Huw Shiel, †‡Oliver S. Hutter, †Laurie J. Phillips, §Mohammed Al Turkestani, †Vin R. Dhanak, †Tim D. Veal, †Ken Durose, †Jonathan D. Major

†Stephenson Institute for Renewable Energy, Department of Physics, University of Liverpool, Liverpool, United Kingdom

§Department of Physics, College of Applied Sciences, Umm Al-Qura University, Makkah, 21955 Makkah, Saudi Arabia

Abstract. The effect of $(NH_4)_2S$ and CS_2 chemical etches on surface chemistry and contacting in Sb_2Se_3 solar cells was investigated via a combination of x-ray photoemission spectroscopy and photovoltaic device analysis. Thin film solar cells were produced in superstrate configuration with an absorber layer deposited by close space sublimation. Devices of up to 5.7% efficiency were compared via current-voltage measurements and temperature-dependent current-voltage analysis. X-ray photoemission spectroscopy analysis demonstrated that both etching processes were successful in removing Sb_2O_3 contamination, while there was no decrease in free elemental selenium content by either etch, in contrast to prior work. Using J-V-T analysis the removal of Sb_2O_3 at the back surface in etched samples was found to improve contacting by reducing the potential barrier at the back contact from 0.43 eV up to 0.26 eV and lowering the series resistance. However, J-V data showed that due to the decrease in shunt resistance and short-circuit current as a result of etching, the devices show a lower efficiency following both etches, despite a lowering of the series resistance. Further optimisation of the etching process yielded an improved efficiency of 6.6%. This work elucidates the role of surface treatments in Sb_2Se_3 devices and resolves inconsistencies in previously published works.

Keywords: Antimony selenide, Sb_2Se_3, Etching, Back contact, Photovoltaics, XPS

1. Introduction

Antimony selenide (Sb_2Se_3) is a rapidly developing inorganic material which shows great promise within the field of thin film photovoltaics (PV); it is a stable, binary V-VI compound with a direct band gap of 1.18 eV [1, 2] well suited for use in PV. Its absorption coefficient is $> 10^5$ cm^{-1} and the constituent materials are cheap and abundant [1] with low toxicity [3]. Sb_2Se_3 adopts a 1-D nanoribbon structure [4] with strong, covalently bonded chains linked by weaker van der Waals bonds. Sb_2Se_3 solar cells are presently an emerging technology with rising efficiencies; the record power conversion

‡ These authors contributed equally to this work

efficiency (PCE) for Sb_2Se_3 devices currently stands at 9.2% [5] and this has improved rapidly from only 2% in 2014 [3, 6]. Impressive device efficiencies have been achieved with a range of device structures and both with and without a variety of interfacial layers. [7, 8, 9, 10] Previous work has shown that device performance depends strongly on the orientation of the nanoribbons in the film and, thus far, a large fraction of work on this material has focused on optimising growth conditions to achieve optimal orientation[4, 5, 6, 10, 11, 12]. As a result there are many aspects of material and device behaviour that are still poorly understood, such as front and back contacting. Sb_2O_3 and free elemental selenium contaminants have been identified at the surface of Sb_2Se_3 films [13, 14], however the impact of this on device behaviour has not yet been properly investigated.

It is well established in other technologies that surface modification prior to back contacting can lead to performance improvement, such as via the nitric-phosphoric acid, [15, 16, 17, 18] bromine methanol [19], methyl ammonium iodide [20] or hydrogen iodide [21] etching step in CdTe solar cells. These etching steps often improve device characteristics through the creation of a Te-rich layer prior to back contacting. It is likewise important to investigate whether an equivalent approach for Sb_2Se_3 can yield similar benefits. Understanding the chemical composition of the free back surface is a key component in developing such a process. In 2017, Wang *et al.* stated that the removal of free elemental selenium using a carbon disulphide (CS_2) etch chemical etchant was successful in increasing the fill factor (*FF*) of their Sb_2Se_3 devices [13]. X-ray photoemission spectroscopy (XPS) analysis showed reduction in Se levels at the surface following the etch treatment. Similarly, Chen *et al.* reported in 2017 that the use of an ammonium sulphide ($(NH_4)_2S$) chemical etch was effective in removing both Sb_2O_3 and Se contamination (also supported by XPS analysis) and that this led to an increase in *FF* [14]. The XPS interpretation, however, was not consistent across the two studies (despite coming from the same group), there being a large discrepancy in the assigned positions of the chemically shifted contaminant peaks (refer to Section 4 for details). Additionally no direct comparison between the etching processes was made as the two studies utilised different Sb_2Se_3 device structures. exact mechanism of the etching processes are unclear - there have been reports on the use of $(NH_4)_2S$ to dissolve Sb-chalcogenides [22] however, to the best of our knowledge, there are no reports on the mechanism of CS_2 as an etchant for Sb_2Se_3. In this work, therefore, we have performed rigorous XPS analysis to accurately determine the effect of the two etches on the Sb_2Se_3 surface and directly link this to changes in the back contact behaviour and device electrical parameters. Importantly, all samples, cells and surfaces were kept consistent throughout the study, with the only variable being the chemical etching process. It is noted that surface passivation layers have been used in the past to improve the performance of Sb_2Se_3 solar cells [10], however these were omitted from this study in order to clarify the role of the etches. This allows us to properly assess the impact and effectiveness of surface treatments for Sb_2Se_3 back contacting for the first time.

Table 1: Tabulated efficiencies of all reported superstrate Sb_2Se_3 solar cells above 5.5% grown by physical vapour deposition techniques.

PCE (%)	Method	Device Structure	Authors	Year
7.6	VTD	ITO/CdS/Sb_2Se_3/Au	Wen et al.[12]	2018
7.5	VTD	ITO/CdS/Sb_2Se_3/HTL/Au	Li et al. [23]	2019
7.5	VTD	ITO/SnO_2/CdS/Sb_2Se_3/Au	Tao et al. [8]	2019
6.84	CSS	FTO/CdS/Sb_2Se_3/HTL/Au	Li et al. [7]	2018
6.63	CSS	FTO/TiO_2/Sb_2Se_3/Au	This Work	2019
6.6	CSS	FTO/TiO_2/Sb_2Se_3/HTL/Au	Hutter et al. [10]	2018
6.5	RTE	ITO/CdS/Sb_2Se_3/HTL/Au	Chen et al. [24]	2017
5.93	RTE	FTO/ZnO/Sb_2Se_3/Au	Wang et al. [13]	2017
5.76	RTE	ITO/CdS/Sb_2Se_3/Au	Liu et al. [25]	2017
5.72	VTD	ITO/CdS/Sb_2Se_3/Au	Hu et al. [26]	2018
5.62	RTE	ITO/CdS/Sb_2Se_3/Au	Zhou et al. [27]	2017
5.6	RTE	FTO/CdS/Sb_2Se_3/Au	Zhou et al. [4]	2015

Sb_2Se_3 samples were deposited by close space sublimation (CSS) - a highly tunable, scalable synthesis method [28]. Sb_2Se_3 solar cells made by CSS have so far achieved efficiencies competitive with the record efficiencies achieved using vapour transport deposition (VTD) and rapid thermal evaporation (RTE) (As shown in Table 1, the use of CSS and the very similar technique of VTD have aided the progression of Sb_2Se_3 to higher efficiencies). Samples were left as an unetched control sample, or were treated with either a CS_2 or an $(NH_4)_2S$ chemical etch to modify the surface chemistry prior to back contacting [13, 14, 29] (Figure 1). Film morphology and crystallinity were investigated by scanning electron microscopy (SEM) and x-ray diffraction (XRD), while the surface chemistry of the back surface was determined using XPS measurements. Devices were produced in the superstrate configuration with a device structure consisting of glass, F:SnO_2, TiO_2, Sb_2Se_3 and Au. Device performance was tested under AM1.5 illumination in order to correlate with changes in surface chemistry. In addition, J-V-T analysis was carried out to measure the change in the back contact barrier height, ϕ_b [30, 31], of the devices with chemical etching.

2. Methods

2.1. Film, Surface and Device Preparation

TiO_2 films were deposited by spin casting titanium isopropoxide onto fluorine-doped tin dioxide coated glass substrates (TEC10 FTO, NSG Group) prior to annealing in air, via

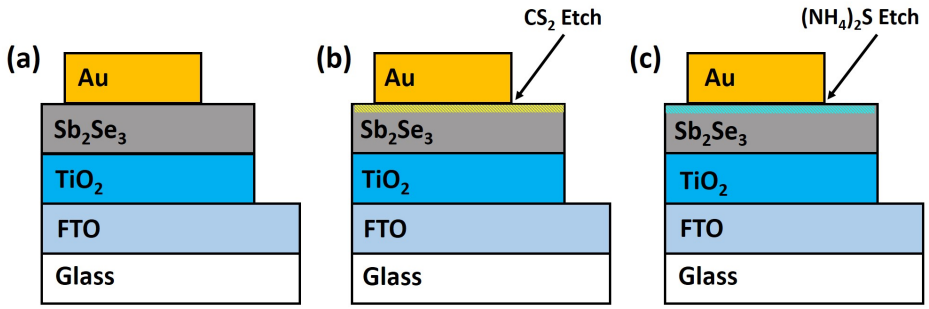

Figure 1: Schematics of device structure for the three studied samples: (a) unetched control sample, (b) CS_2-etched sample and (c) $(NH_4)_2S$-etched sample.

an established two-step process [32]. Sb_2Se_3 was then deposited via a multi-step CSS process [10] utilising a seed layer deposited at a pressure of 10^{-2} mbar, followed by a thicker layer with a source temperature of 470°C for 15 minutes at a pressure of 13 mbar N_2 to give a total layer thickness of $\sim$2 μm. This process was developed to generate layers with a more compact grain structure. In addition to an unetched control sample, two surface treatments were used, these being a CS_2 etch and an $(NH_4)_2S$ etch. For the CS_2 etch, a 25 mm $\times$ 25 mm sample was rinsed with 3 ml of CS_2 as carried out by Wang *et al.* [13]. For the $(NH_4)_2S$-etched sample, 3 ml of 0.3 mmol.dm^{-3} $(NH_4)_2S$ (aqueous), and subsequently 3 ml of H_2O, was applied to the substrate using a spin coater at 2500 rpm, as described by Chen *et al.* [14]. For completion of devices, 100nm thick Au back contacts were then thermally evaporated through a shadow mask, creating $N = 16$ cells per sample type, each having an active area of 0.1 cm^2. Figure 1 shows a schematic diagram of the device structure.

2.2. Materials and Device Characterisation

SEM images were taken using a JEOL 7001F with an acceleration voltage of 5 kV. XRD was performed with a Rigaku SmartLab x-ray diffractometer in a parallel beam configuration. XPS measurements were performed inside an ultra-high vacuum chamber operating at a pressure less than 4×10^{-9} mbar. Samples were secured to a sample plate using double sided carbon tape and a narrow strip of tantalum connecting the surface to the plate, to prevent charging. The surface composition was probed using core-level-XPS with a Mg Kα x-ray source (hν = 1253.6 eV) operating at 200 W and a hemispherical Scienta SES200 electron energy analyser comprised of a double channel plate and phosphor screen with a CCD camera. The resolution was determined from the full width at half maximum (FWHM) of a Ag $3d_{5/2}$ peak of a Ag calibration sample to be 0.7 eV, allowing binding energy determination with a precision of $\pm$ 0.1 eV.

Device performance was measured under simulated AM1.5 illumination at 1000 W m^{-2} using a TS Space Systems solar simulator and a Keithley 2400 source-meter. The Au/Sb_2Se_3 back-contact barrier height, ϕ_b, was determined from dark J-V measurements

as a function of temperature (J-V-T) using a CTI-cryogenics cryostat in the range 250-350K, with J-V curves taken using a Keithley 2400 source-meter over the range -1 to 1 V. Using the method proposed by Bätzner *et al.*[31], the series resistance, R_s, is determined at forward bias above open-circuit voltage (V_{oc}) as a function of temperature i.e. the slope method. $R_s(T)$ may then be separated into an invariant, an Ohmic and an exponential component, the latter resulting from the passage of the carriers over the back contact via thermionic emission. R_s is thereby expressed as follows:

$$R_s = R_{\Omega 0} + \frac{\partial R_{\Omega 0}}{\partial T} T + \frac{C}{T^2} exp\left(\frac{\phi_b}{\mathrm{k}T}\right) \tag{1}$$

where C is a fitting parameter, $R_{\Omega 0}$ is the Ohmic resistance, and k is the Boltzmann constant. As shown by Al Turkestani [30], at low temperature the exponential term is much greater than the first two terms. Hence, for this experiment, the third term is deemed sufficient and the expression is simplified to:

$$R_s \approx \frac{C}{T^2} exp\left(\frac{\phi_b}{\mathrm{k}T}\right) \tag{2}$$

3. Results

3.1. Film Morphology

SEM images of as-deposited and etched films are shown in Figure 2. It can be seen that the films have large and reasonably uniform grains (up to 2 μm across), with some cavities visible at the surface owing to the large grain structure. The etches have little obvious impact on the surface morphology, aside from some loss of delineation of the grain boundaries following the $(NH_4)_2S$ etch (Figure 2c).

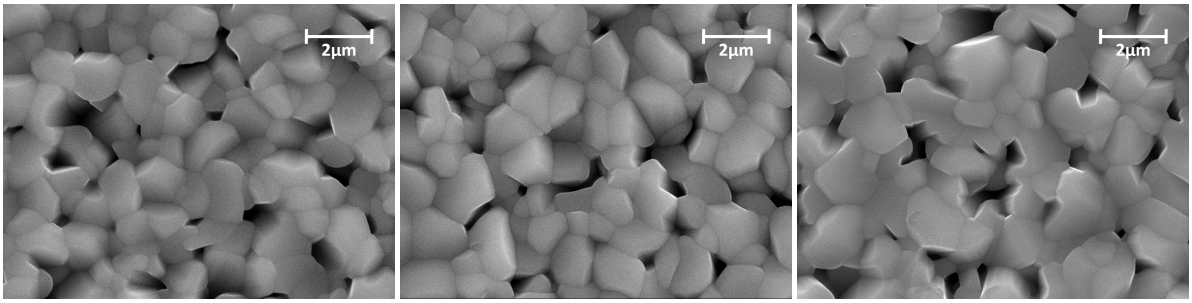

(a) Unetched Sb_2Se_3 film (b) CS_2-etched Sb_2Se_3 film (c) $(NH_4)_2S$-etched Sb_2Se_3 film

Figure 2: SEM micrographs of (a) unetched control, (b) CS_2-etched and (c) $(NH_4)_2S$-etched Sb_2Se_3 films.

Similar to SEM analysis, XRD patterns (Figure 3) show no significant differences between the samples, with all three patterns showing prominent peaks at 28.2°, 31.2°, 32.2° and 45.6° that are characteristic of the (211), (221), (301) and (002) planes

respectively (using the Pbnm space-group labeling convention [11]). These planes are representative of nanoribbons lying at 37°, 44°, 46° and 0° from normal to the substrate for the (211), (221), (301) and (002) planes respectively. Growth of nanoribbons normal to the substrate surface would be expected to optimise both vertical conduction along the nanoribbon axes and also increase the fraction of van der Waals-bonded rather than covalent-bonded grain boundaries, both of which are expected to be beneficial to photovoltaic performance [2, 4]. Even the ∼45° angle of the (221) and (301) planes from normal is not expected to impede carrier transport due to the size of the grains in this material. It is reasonable to assume that the majority of the grains, and therefore the nanoribbons, span from the bottom to the top of the film [2, 11]. There is a small difference in the peak at 26.6°, however this is attributed to an additional Sb_2Se_3 (021) orientation [2] and is therefore not indicative of any significant change at the surface.

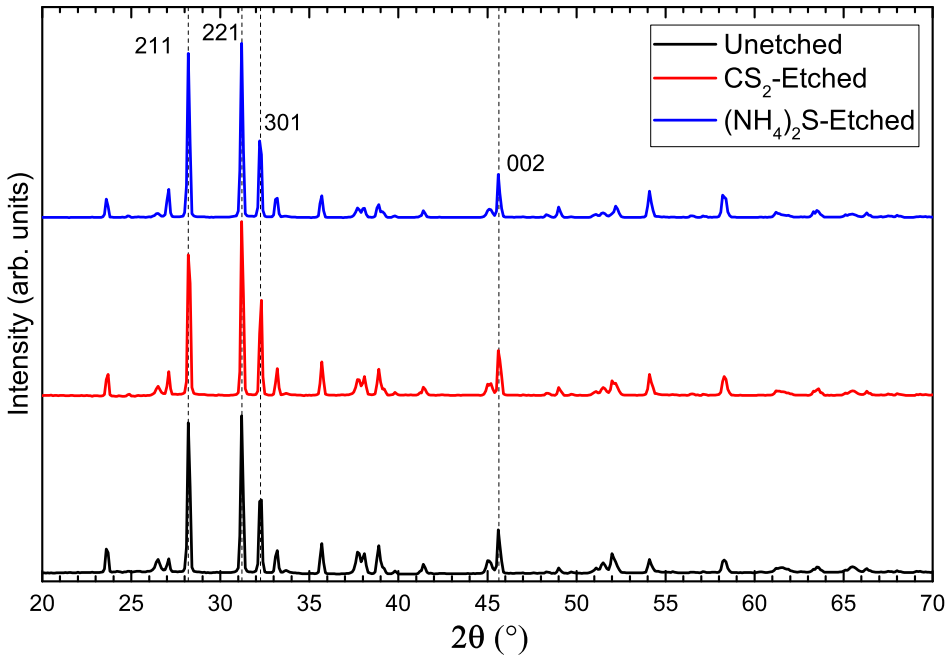

Figure 3: XRD patterns of unetched, CS_2-etched, and $(NH_4)_2S$-etched Sb_2Se_3 samples showing prominent peaks at 28.2°, 31.2°, 32.2° and 45.6°.

Overall the SEM and XRD studies revealed that the etching processes introduced no significant morphological or crystallographic change that was detectable using these methods. Therefore, the surface sensitivity of XPS was required to detect the important chemical changes.

3.2. Surface Chemistry

Figures 4 & 5 show the XPS spectra for the Sb 4d (30 - 40 eV) and Se 3d (50 - 60 eV) regions respectively, for each of the unetched, CS_2-etched and $(NH_4)_2S$-etched samples. For the Sb 4d region, three chemical species were identified: Sb_2Se_3, Sb_2O_3 and metallic Sb [33, 34, 35, 36]. The oxide component was determined to be Sb_2O_3 and not Sb_2O_5

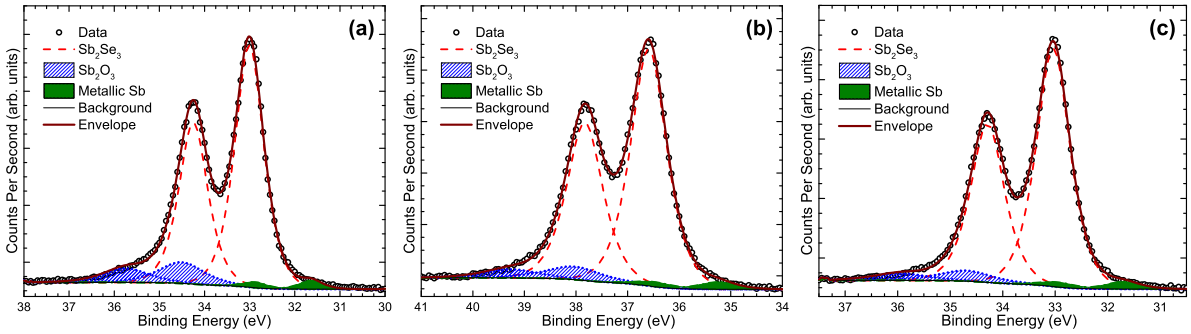

(a) Unetched (b) CS_2-etched (c) $(NH_4)_2S$-etched

Figure 4: XPS spectra of Sb 4d regions for (a) unetched (b) CS_2-etched and (c) $(NH_4)_2S$-etched Sb_2Se_3 films. It can be seen that the relative amount of Sb_2O_3 is reduced with etching. There is also a low, unchanged metallic antimony signal in all three samples.

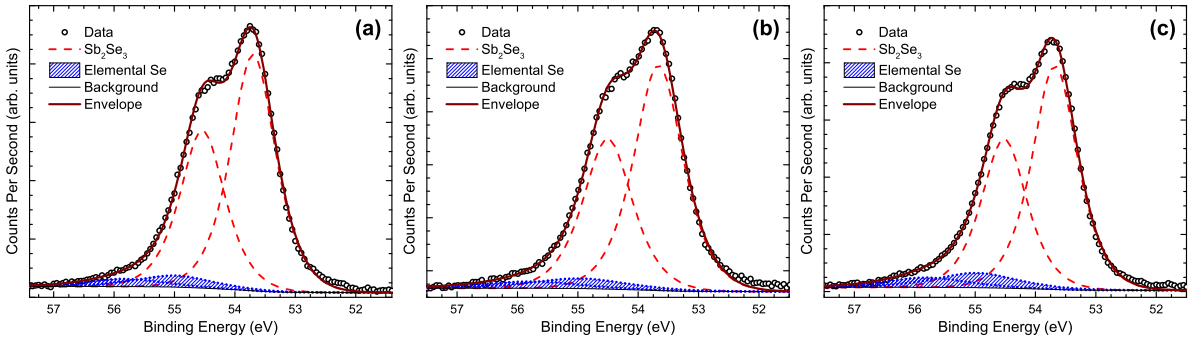

(a) Unetched (b) CS_2-etched (c) $(NH_4)_2S$-etched

Figure 5: XPS spectra of Se 3d regions for (a) unetched (b) CS_2-etched and (c) $(NH_4)_2S$-etched Sb_2Se_3 films. It can be seen that the relative amount of free elemental selenium rises with the $(NH_4)_2S$ etch but is unchanged by the CS_2 etch.

or a mix of the two species due to a clear difference in chemical shift (∼1 eV) for the two species relative to Sb_2Se_3 [34, 35]. For the Se 3d region, two chemical species were identified: Sb_2Se_3 and free elemental Se [13, 34, 37, 38]. The binding energies of the components are displayed in Table 2. As only relative quantities can be determined from peak areas in XPS analysis, all contamination levels are presented as percentages of the Se or Sb present at the surface in each of their chemical environments (Table **??** & Figure 6). For example, the amount of free elemental selenium present is characterised as the amount of free elemental selenium as a percentage of total selenium detected in all its environments.

In Figure 4, although the magnitude of the signal is understandably dwarfed by the Sb_2Se_3 signal, it is noticeable that the Sb_2O_3 peaks are reduced in size after etching with both CS_2 and $(NH_4)_2S$, indicating removal of the oxide via etching. However, it

Table 2: Identified peaks in the XPS spectra for Sb_2Se_3 samples.

Peak	Measured Binding Energy (eV)	FWHM
Sb(Se) $4d_{5/2}$	33.0	0.8
Sb(Se) $4d_{3/2}$	34.2	0.8
Sb(O) $4d_{5/2}$	34.5	1.1
Sb(O) $4d_{3/2}$	35.7	1.1
Sb $4d_{5/2}$	31.6	0.7
Sb $4d_{3/2}$	32.9	0.7
Se(Sb) $3d_{5/2}$	53.7	0.9
Se(Sb) $3d_{3/2}$	54.5	0.9
Se $3d_{5/2}$	55.0	1.5
Se $3d_{3/2}$	55.8	1.5

is also noted that here the level of contamination is already very low in the unetched sample compared with the other unetched samples previously reported by Wang *et al.* and Chen *et al.* [13, 14]. The CSS deposition technique used in this work uses an inert nitrogen atmosphere and samples were exposed to air for minimal time (< 30 minutes) between deposition and XPS measurement. A low level of contamination is therefore consistent with our expectations.

The levels of Se and Sb_2O_3 contamination are summarized in Table S1 and Figure 6. It is clear that both etching processes reduce the level of Sb_2O_3 contamination, with the $(NH_4)_2S$ etch being marginally more effective. However, while the CS_2 etch has little or no effect on the amount of free elemental selenium at the back contact surface, the $(NH_4)_2S$ etch increases the proportion of free elemental selenium at the surface. This indicates that the etches do not selectively remove selenium and in the case of the $(NH_4)_2S$ etch it in fact produces a more selenium rich surface. In this work, by ensuring consistency in the fitting procedure used to analyse the effect of both etches, we show beyond doubt that the primary result of the etch process is Sb_2O_3 removal and not Se removal. This is contrary to previous work, in which inconsistencies in the XPS fitting procedure led to misidentification of Se removal as the primary result of the CS_2 etching process [13] [14] (as discussed in Section 4). The next step is then to determine what impact this has on the device contacting and performance.

3.3. Device Performance and Contact Barrier Height Determination

A series of complete cells were produced with absorber layers and etching steps identical to those used for XPS analysis to allow direct comparison. Average and peak device performance parameters extracted from J-V analysis are shown in Tables 3 & 4 for an unetched sample and samples etched by CS_2 and $(NH_4)_2S$. Here it can be seen that

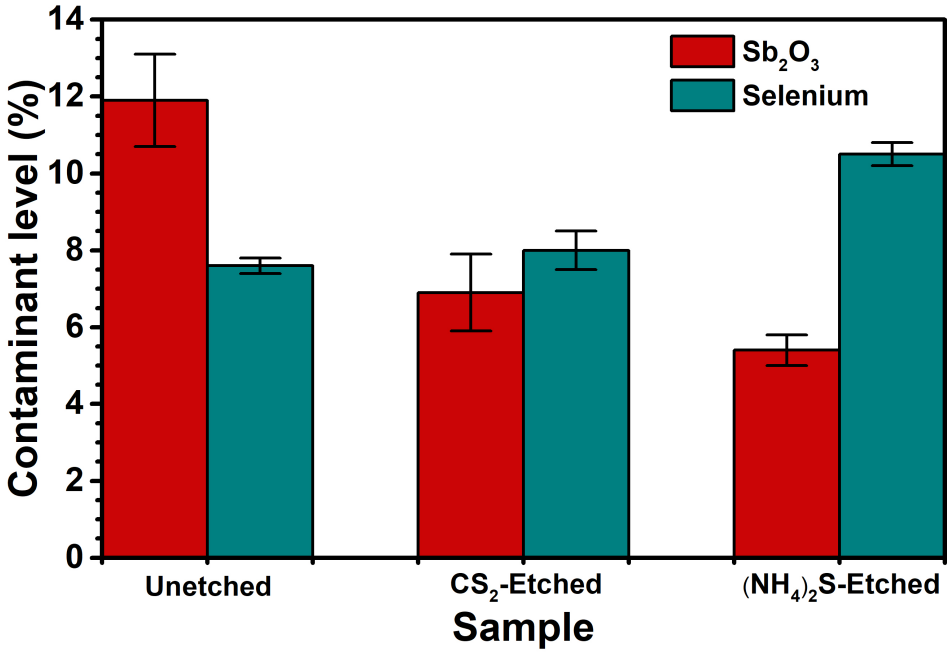

Figure 6: Sb_2O_3 and selenium contamination levels with different etches. Both etches reduce the proportion of oxide contamination, while relative levels of free elemental selenium rise slightly with the $(NH_4)_2S$ etch but are unchanged by the CS_2 etch.

Table 3: Average J-V results and standard deviations for devices with different chemical etch treatments ($N = 16$ per device type).

Device	PCE (%)	V_{oc} (V)	J_{sc} (mA.cm^{-2})	FF (%)
Unetched	5.00 ($\pm$0.46)	0.42 ($\pm$0.01)	28.2 ($\pm$2.1)	42.4 ($\pm$1.1)
CS_2	4.27 ($\pm$1.68)	0.36 ($\pm$0.09)	27.1 ($\pm$2.8)	40.7 ($\pm$8.2)
$(NH_4)_2S$	3.73 ($\pm$1.58)	0.37 ($\pm$0.11)	21.8($\pm$5.4)	42.2 ($\pm$8.0)

chemical etching has a negative effect on both the average and peak performances of the device. The main differences occur in V_{oc} and J_{sc}, with the $(NH_4)_2S$ etch being especially harmful to the J_{sc}.

Table 4: Peak J-V results for devices with different chemical etch treatments.

Device	PCE (%)	V_{oc} (V)	J_{sc} (mA.cm^{-2})	FF (%)	R_s (Ω.cm^{-2})	R_{sh} (Ω.cm^{-2})
Unetched	5.70	0.42	30.7	44.2	5.0	73.5
CS_2	5.55	0.40	29.2	47.5	4.8	72.3
$(NH_4)_2S$	4.89	0.42	25.1	46.4	3.9	68.2

In the peak performing cells, both etches see a reduction in R_s at high forward bias, with the reduction being greater in the $(NH_4)_2S$-etched device. This correlates well with the removal of oxide seen in the XPS spectra. There is also a reduction in shunt resistance (R_{sh}) following both etches which suggests some damage to the film by the etches leading to and increase in shunting pathways. This is suported by the loss in J_{sc} caused by both etches, in particular the $(NH_4)_2S$ etch which sees the greatest reduction in R_{sh}.

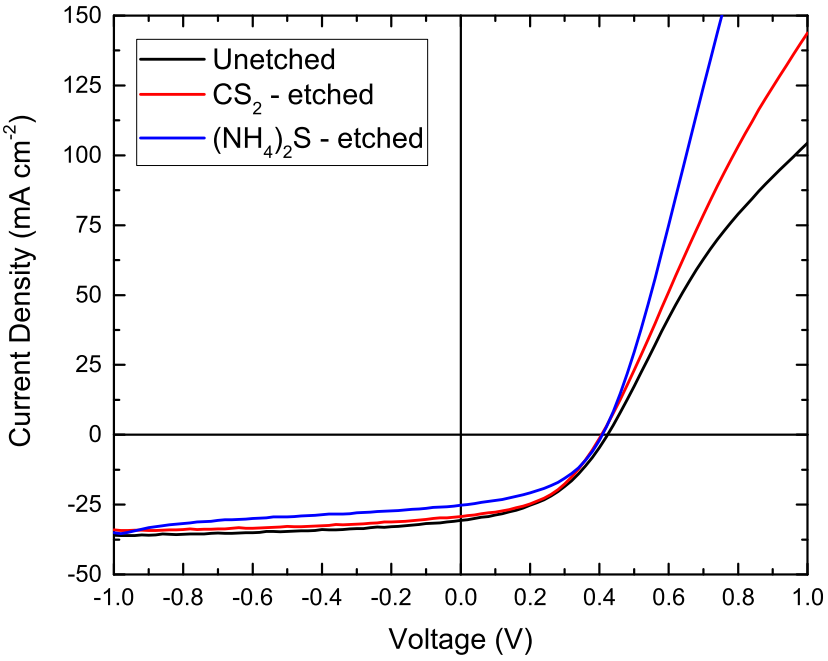

Figure 7: J-V scans for the best performing Sb_2Se_3 devices with no etching treatment, CS_2 etch and $(NH_4)_2S$ etch

J-V-T analysis was carried out on all CSS deposited Sb_2Se_3 devices in order to determine the magnitude of ϕ_b. R_s values were measured in the dark via the slope method for a range of temperatures (250 - 350 K) for all devices prior to fitting them using Equation 2. The fits can be found in Figure 8 and the results of the fitting are shown in Table 5. The results show that the barrier height is lowered by both etches, with a similar decrease for both the $(NH_4)_2S$ etch and the CS_2 etch (albeit slightly larger for the CS_2). This correlates well with the XPS results and the device results, indicating that a removal of the oxide layer is beneficial to the back contact performance. [13, 14].

4. Discussion

The impact of $(NH_4)_2S$ etch and CS_2 etches on Sb_2Se_3 identified here is notably different from prior reports [13, 14]. Wang *et al.* [13] suggested CS_2 improved *FF* by dramatically reducing the proportion of free elemental selenium at the back contact. However, in this

Table 5: Measured back contact barriers for Sb_2Se_3 devices.

Sb_2Se_3 Surface Treatment	Barrier Height (eV)
Unetched	0.43 ±0.01
CS_2-etched	0.26 ±0.01
$(NH_4)_2S$-etched	0.29 ±0.01

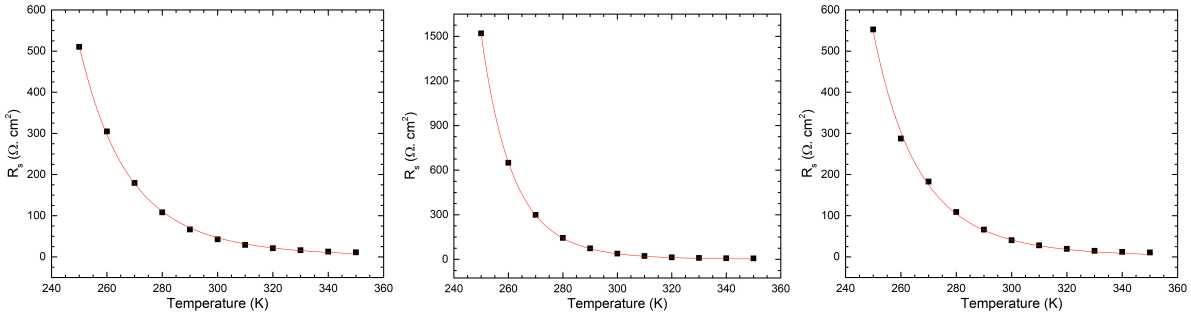

(a) Unetched (b) CS_2-etched (c) $(NH_4)_2S$-etched

Figure 8: R_s data with exponential fit used to calculate back contact barrier height in (a) unetched, (b) CS_2-etched and (c) $(NH_4)_2S$-etched Sb_2Se_3 devices.

work we observe a reduction in Sb_2O_3 and not elemental selenium to be the primary role of CS_2 etching. This discrepancy in the effect on selenium can be explained, in part, by the much lower selenium contamination levels in our devices (Figure 5) due to use of a CSS process rather than vapour transport deposition (as used by Wang *et al.* and Chen *et al*) and may be the reason why they see a greater influence on device performance[13, 14]. Chen *et al.* reported that the $(NH_4)_2S$ etch effectively removes both Sb_2O_3 and free elemental selenium from the back contact [14]. However, the XPS peak fitting of the Se region by Chen *et al.* was dramatically inconsistent with both Wang *et al.*[13] and this work. In this work, the binding energy separation between elemental Se and Sb_2Se_3 in the Se region is ∼1.3 eV, consistent with Wang *et al.*, and other reports [13, 34, 37]. However, Chen *et al.* [14] state this separation as ∼0.6 eV, combined with a very broad line shape for the alleged elemental Se component. Given the 0.1 eV precision of binding energy determination in XPS, this difference casts doubt over the validity of these assignments, and therefore it cannot be concluded from their work that the $(NH_4)_2S$ treatment is in fact effective in removing free elemental selenium. Indeed our results show there to be no removal of elemental selenium and the improvement they observed in device performance is most likely due to removal of Sb_2O_3, which would be consistent with the work carried out in this study.

Our results indicate that while these chemical etches have led to an improvement in device performance in previous studies they are in some cases harmful [13, 14]. The removal of Sb_2O_3 from the back contact decreases the barrier height and lowers the series

resistance, however the decrease in J_{sc} and R_{sh} in J-V measurements can be explained by damage to the film upon etching. Whilst it is likely that the removal of a resistive Sb_2O_3 layer would benefit device performance by lowering of the series resistance and increasing the FF, there are clear differences in the initial level of contamination on the surfaces of our samples compared to those of Wang *et al.* and Chen *et al.* [13, 14]. Our samples show very low levels of Sb_2O_3 and free elemental selenium contamination compared to those shown in the previous studies, presumably due to the different deposition method. For example, the RTE process uses no inert gas during deposition and also deposits at a much higher rate than CSS and at a different pressure ($\sim$ 0.01 mbar rather than $\sim$ 13 mbar) [4]. Additionally, in the RTE process the Sb_2Se_3 melts before evaporating, whereas in CSS the material directly sublimes onto the substrate which could lead to differences in contamination from the source material [4]. It seems likely therefore that the state of the as-deposited Sb_2Se_3 surface plays a major role in the effectiveness of these chemical etches. We postulate that if the sample has a thick layer of Sb_2O_3 contamination then the etches are effective in reducing the thickness of a resistive layer, thereby improving the fill factor of the device. However, if the Sb_2O_3 layer is very thin, the reduction in R_s is counteracted by a more significant decrease in R_{sh} and J_{sc} that lowers the overall performance of the cell. This is supported by the fact that EQE measurements show that the $(NH_4)_2S$-etched sample has uniformly lower EQE across all wavelengths whilst showing no change in shape in the EQE spectrum (Figure S1).

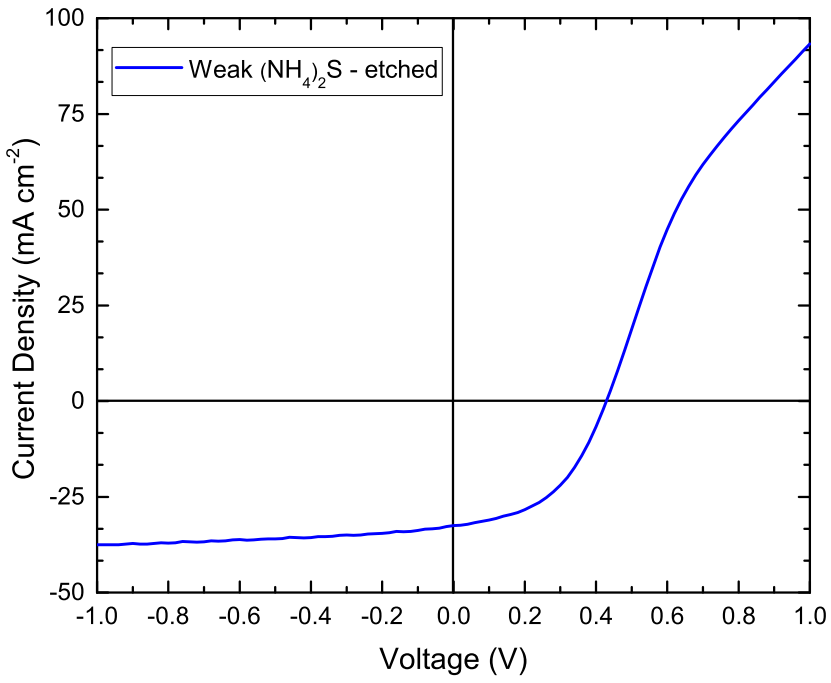

Figure 9: J-V curve of a device etched with a more dilute (0.03 mmol.dm^{-3}) solution of $(NH_4)_2S$ showing improved performance from that shown in Figure 7.

Building on these conclusions, a more dilute treatment of the $(NH_4)_2S$ etch was applied using the same process as previously described but with a concentration of 0.03 mmol.dm^{-3}. This succeeded in improving the device performance to over 6.6%, as shown in Figure 9 (PCE = 6.63%, V_{oc} = 0.42 V, J_{sc} = 32.5 mA.cm^{-2}, FF = 48.5), which further supports the conclusions of this work and shows a way forward in optimising back contact treatments for Sb_2Se_3 solar cells.

5. Conclusion

This work shows with clarity the benefits and drawbacks of etching prior to application of the back contact for Sb_2Se_3 solar cells and resolves inconsistencies in the literature. XPS analysis of the back surface shows a reduction of Sb_2O_3 contamination from both etches. J-V-T analysis reveals a significant decrease in potential barrier at the back contact upon etching, from 0.43 to 0.29 eV with the $(NH_4)_2S$ etch, likely as a result of Sb_2O_3 removal. J-V analysis reveals a decrease in series resistance after etching which can be attributed to the presence of a smaller amount of resistive Sb_2O_3. Additionally, there is an decrease in J_{sc} and overall efficiency following both etches due to damage of the film. Upon diluting the $(NH_4)_2S$ etch, device efficiency was improved to 6.6%. Overall, the study clarifies the role of the etches in removing surface contamination, showing a more varied result when the initial deposition conditions are changed, and provides insight into the way forward in optimising Sb_2Se_3 back contacts.

6. Acknowledgements

The Engineering and Physical Sciences Research Council (EPSRC) is acknowledged for funding of H.S. (Grant No. EP/N509693/1), O.S.H. and K.D. (Grant No. EP/M024768/1), L.J.P. and J.D.M. (Grant No. EP/N014057/1), and V.R.D. and T.D.V. (Grant No. EP/N015800/1). The XRD facility was supported by the EPSRC under Grant No. EP/P001513/1. Paul Warren of NSG Group is thanked for discussions, funding of H.S. and for supplying coated glass substrates.

7. References

[1] C. Chen, W. Li, Y. Zhou, C. Chen, M. Luo, X. Liu, K. Zeng, B. Yang, C. Zhang, J. Han, J. Tang, Optical properties of amorphous and polycrystalline Sb_2Se_3 thin films prepared by thermal evaporation, Applied Physics Letters 107 (4) (2015) 043905. doi:10.1063/1.4927741.

[2] M. Birkett, W. M. Linhart, J. Stoner, L. J. Phillips, K. Durose, J. Alaria, J. D. Major, R. Kudrawiec, T. D. Veal, Band gap temperature-dependence of close-space sublimation grown Sb_2Se_3 by photo-reflectance, APL Materials 6 (8) (2018) 084901. doi:10.1063/1.5027157.

[3] M. Luo, M. Leng, X. Liu, J. Chen, C. Chen, S. Qin, J. Tang, Thermal evaporation and characterization of superstrate CdS/Sb_2Se_3 solar cells, Applied Physics Letters 104 (17) (2014) 173904. doi:10.1063/1.4874878.

[4] Y. Zhou, L. Wang, S. Chen, S. Qin, X. Liu, J. Chen, D. J. Xue, M. Luo, Y. Cao, Y. Cheng, E. H. Sargent, J. Tang, Thin-film Sb_2Se_3 photovoltaics with oriented one-dimensional ribbons and benign grain boundaries, Nature Photonics 9 (6) (2015) 409–415. doi:10.1038/nphoton.2015.78.

[5] Z. Li, X. Liang, G. Li, H. Liu, H. Zhang, J. Guo, J. Chen, K. Shen, X. San, W. Yu, R. E. I. Schropp, Y. Mai, 9.2%-Efficient Core-Shell Structured Antimony Selenide Nanorod Array Solar Cells, Nature Communications 10 (125) (2019) 1–9. doi:10.1038/s41467-018-07903-6.

[6] X, Liu et al, Thermal evaporation and characterization of Sb_2Se_3 thin film for substrate Sb_2Se_3/CdS solar cells, ACS Applied Materials & Interfaces 6 (2014) 10687–10695. doi:10.1021/am502427s.

[7] D.-B. Li, X. Yin, C. R. Grice, L. Guan, Z. Song, C. Wang, C. Chen, K. Li, A. J. Cimaroli, R. A. Awni, D. Zhao, H. Song, W. Tang, Y. Yan, J. Tang, Stable and efficient CdS/Sb_2Se_3 solar cells prepared by scalable close space sublimation, Nano Energy 49 (2018) 346 – 353. doi:https://doi.org/10.1016/j.nanoen.2018.04.044.

[8] J. Tao, X. Hu, Y. Guo, J. Hong, K. Li, J. Jiang, S. Chen, C. Jing, F. Yue, P. Yang, C. Zhang, Z. Wu, J. Tang, J. Chu, Solution-processed SnO_2 interfacial layer for highly efficient Sb_2Se_3 thin film solar cells, Nano Energy 60 (2019) 802 – 809. doi:https://doi.org/10.1016/j.nanoen.2019.04.019.

[9] C. Chen, K. Li, S. Chen, L. Wang, S. Lu, Y. Liu, D. Li, H. Song, J. Tang, Efficiency improvement of Sb_Se_3 solar cells via grain boundary inversion, ACS Energy Letters 3 (10) (2018) 2335–2341. doi:10.1021/acsenergylett.8b01456.

[10] O. S. Hutter, L. J. Phillips, K. Durose, J. Major, 6.6% efficient antimony selenide solar cells using grain structure control and an organic contact layer, Solar Energy Materials Solar Cells 188 (2018) 177 – 181. doi:10.1016/j.solmat.2018.09.004.

[11] L. J. Phillips, C. N. Savory, O. S. Hutter, P. J. Yates, H. Shiel, S. Mariotti, L. Bowen, M. Birkett, K. Durose, D. O. Scanlon, J. D. Major, Current enhancement via a TiO_2 window layer for CSS Sb_2Se_3 solar cells: performance limits and high V_{oc}, IEEE Journal of Photovoltaics 9 (2). doi:10.1109/JPHOTOV.2018.2885836.

[12] X. Wen, C. Chen, S. Lu, K. Li, R. Kondrotas, Y. Zhao, W. Chen, L. Gao, C. Wang, J. Zhang, G. Niu, J. Tang, Vapor transport deposition of antimony selenide thin film solar cells with 7.6% efficiency, Nature Communications 9 (2018) 2179. doi:10.1038/s41467-018-04634-6.

[13] L. Wang, D. B. Li, K. Li, C. Chen, H. X. Deng, L. Gao, Y. Zhao, F. Jiang, L. Li, F. Huang, Y. He, H. Song, G. Niu, J. Tang, Stable 6%-efficient Sb_2Se_3 solar cells with a ZnO buffer layer, Nature Energy 2 (4) (2017) 17046. doi:10.1038/nenergy.2017.46.

[14] C. Chen, Y. Zhao, S. Lu, K. Li, Y. Li, B. Yang, W. Chen, L. Wang, D. Li, H. Deng, F. Yi, J. Tang, Accelerated optimization of TiO_2/Sb_2Se_3 thin film solar cells by high-throughput combinatorial approach, Advanced Energy Materials 7 (20) (2017) 1700866. doi:10.1002/aenm.201700866.

[15] J. D. Major, R. E. Treharne, L. J. Phillips, K. Durose, A low-cost non-toxic post-growth activation step for CdTe solar cells, Nature 511 (7509) (2014) 334–337. doi:10.1038/nature13435.

[16] T. Baines, G. Zoppi, L. Bowen, T. P. Shalvey, S. Mariotti, K. Durose, J. D. Major, Incorporation of CdSe layers into CdTe thin film solar cells, Solar Energy Materials and Solar Cells 180 (2018) 196 – 204. doi:10.1016/j.solmat.2018.03.010.

[17] Y. Y. Proskuryakov, K. Durose, B. M. Taele, G. P. Welch, S. Oelting, Admittance spectroscopy of CdTeCdS solar cells subjected to varied nitric-phosphoric etching conditions, Journal of Applied Physics 101 (1) (2007) 014505. doi:10.1063/1.2402961.

[18] Y. Kwon, J. Seo, Y. Kang, D. Kim, J. Kim, Bifacial CdS/CdTe thin-film solar cells using a transparent silver nanowire/indium tin oxide back contact, Opt. Express 26 (2) (2018) A30–A38. doi:10.1364/OE.26.000A30.

[19] S. G. Kumar, K. S. R. K. Rao, Physics and chemistry of CdTe/CdS thin film heterojunction photovoltaic devices: fundamental and critical aspects, Energy Environ. Sci. 7 (2014) 45–102. doi:10.1039/C3EE41981A.
URL `http://dx.doi.org/10.1039/C3EE41981A`

[20] S. C. Watthage, A. B. Phillips, G. K. Liyanage, Z. Song, J. M. Gibbs, F. K. Alfadhili, R. B. Alkhayat, R. H. Ahangharnejhad, Z. S. Almutawah, K. P. Bhandari, R. J. Ellingson, M. J. Heben, Selective cd removal from CdTe for high-efficiency te back-contact formation, IEEE Journal of Photovoltaics 8 (4) (2018) 1125–1131. doi:10.1109/JPHOTOV.2018.2830302.

[21] R. A. Awni, D.-B. Li, C. R. Grice, Z. Song, M. A. Razooqi, A. B. Phillips, S. S. Bista, P. J. Roland, F. K. Alfadhili, R. J. Ellingson, M. J. Heben, J. V. Li, Y. Yan, The effects of hydrogen iodide back surface treatment on CdTe Solar cells, Solar RRL 3 (3) (2019) 1800304. doi:10.1002/solr.201800304.

[22] Z. Xia, J. Zhong, M. Leng, L. Hu, D.-J. Xue, B. Yang, Y. Zhou, X. Liu, S. Qin, Y.-B. Cheng, J. Tang, Generalized water-processed metal chalcogenide complexes: Synthesis and applications, Chemistry of Materials 27 (23) (2015) 8048–8057. doi:10.1021/acs.chemmater.5b03614.

[23] K. Li, S. Wang, C. Chen, R. Kondrotas, M. Hu, S. Lu, C. Wang, W. Chen, J. Tang, 7.5% nip sb2se3 solar cells with cuscn as a hole-transport layer, J. Mater. Chem. A 7 (2019) 9665–9672. doi:10.1039/C9TA01773A.

[24] C. Chen, L. Wang, L. Gao, D. Nam, D. Li, K. Li, Y. Zhao, C. Ge, H. Cheong, H. Liu, H. Song, J. Tang, 6.5% certified efficiency Sb_2Se_3 solar cells using PbS colloidal quantum dot film as hole-transporting layer, ACS Energy Letters 2 (9) (2017) 2125–2132. doi:10.1021/acsenergylett.7b00648.

[25] X. Liu, X. Xiao, Y. Yang, D.-J. Xue, D.-B. Li, C. Chen, S. Lu, L. Gao, Y. He, M. C. Beard, G. Wang, S. Chen, J. Tang, Enhanced sb2se3 solar cell performance through theory-guided defect control, Progress in Photovoltaics: Research and Applications 25 (10) (2017) 861–870. doi:10.1002/pip.2900.

[26] X. Hu, J. Tao, S. Chen, J. Xue, G. Weng, Kaijiang, Z. Hu, J. Jiang, S. Chen, Z. Zhu, J. Chu, Improving the efficiency of sb2se3 thin-film solar cells by post annealing treatment in vacuum condition, Solar Energy Materials and Solar Cells 187 (2018) 170 – 175. doi:https://doi.org/10.1016/j.solmat.2018.08.006.

[27] Y. Zhou, Y. Li, J. Luo, D. Li, X. Liu, C. Chen, H. Song, J. Ma, D.-J. Xue, B. Yang, J. Tang, Buried homojunction in cds/sb2se3 thin film photovoltaics generated by interfacial diffusion, Applied Physics Letters 111 (1) (2017) 013901. doi:10.1063/1.4991539.

[28] O. S. Hutter, L. J. Phillips, P. J. Yates, J. D. Major, K. Durose, CSS antimony selenide film morphology and high efficiency PV devices, WCPEC-7 Conference Paper-doi:10.1109/PVSC.2018.8547653.

[29] P. Walker, W. H. Tarn, Handbook of Metal Etchants, CRC Press, 1991.

[30] M. Al Turkestani, CdTe solar cells: key layers and electrical effects, Ph.D. thesis, Durham University (2010).

[31] D. L. Bätzner, M. E. Öszan, D. Bonnet, K. Bücher, Device analysis methods for physical cell parameters of CdTe/CdS solar cells, Thin Solid Films 361 (2000) 288–292. doi:10.1016/S0040-6090(99)00862-7.

[32] S. Mariotti, O. S. Hutter, L. J. Phillips, P. J. Yates, B. Kundu, K. Durose, Stability and performance of $CsPbI_2Br$ thin films and solar cell devices, ACS Applied Materials & Interfaces 10 (4) (2018) 3750–3760. doi:10.1021/acsami.7b14039.

[33] D.-H. Kim, S.-J. Lee, M. S. Park, J.-K. Kang, J. H. Heo, S. H. Im, S.-J. Sung, Highly reproducible planar Sb_2S_3-sensitized solar cells based on atomic layer deposition, Nanoscale 6 (23) (2014) 14549–14554. doi:10.1039/C4NR04148H.

[34] J. F. Moulder, W. F. Stickle, P. E. Sobol, K. D. Bomben, Handbook of X-ray Photoelectron Spectroscopy, Perkin-Elmer Corporation, (1992).

[35] C. D. Wagner, Chemical shifts of Auger lines, and the Auger parameter, Faraday Discussions of the Chemical Society 60 (1975) 291–300. doi:10.1039/DC9756000291.

[36] W. E. Morgan, W. J. Stec, J. R. Van Wazer, Inner-orbital binding-energy shifts of antimony and bismuth compounds, Inorganic Chemistry 12 (4) (1973) 953–955. doi:10.1021/ic50122a054.

[37] R. J. Mehta, C. Karthik, W. Jiang, B. Singh, Y. Shi, R. W. Siegel, T. Borca-Tasciuc, G. Ramanath, High electrical conductivity antimony selenide nanocrystals and assemblies, Nano Letters 10 (11) (2010) 4417–4422. doi:10.1021/nl1020848.

[38] G. Malmsten, I. Thorn, S. Hgberg, J.-E. Bergmark, S.-E. Karlsson, E. Rebane, Selenium compounds studied by means of ESCA, Physica Scripta 3 (2) (1971) 96.